



Nondestructive analysis techniques for freeze-thaw damage detection in concrete slabs using shear waves

Katelyn Freese^{*}, Lev Khazanovich, Kyle Hoegh

Iowa State University, United States

University of Pittsburgh, United States

Minnesota Department of Transportation, United States

Received 16 January 2018; received in revised form 18 June 2018; accepted 24 June 2018

Abstract

Freeze-thaw damage in concrete structures is a serious issue for infrastructure in cold regions. Accurate detection of this type of damage at early stages allows for the selection of optimum strategies for preservation and rehabilitation activities. This paper explores the feasibility of utilizing ultrasonic shear wave technology, called MIRA, for quantification of damage in concrete slabs for the detection of freeze-thaw damage. Four slabs with varying levels of freeze-thaw damage were tested and two analysis techniques were developed to characterize the damage present. These methods involve the formulation of reconstruction images to analyze the subsurface condition, as well as the creation of a numerical index based upon recorded shear wave signal characteristics. The results of both analyses showed agreement both with each other and with the visual survey assessments for detection of freeze-thaw damage. However, the methods were also able to detect damage in portions of the slab where no visual cracks were observed. These techniques showed promise for an accurate nondestructive quantification of the extent of freeze-thaw damage, or similar damage manifestations, in concrete structures. Advantages of the methods include their applicability on in-situ concrete infrastructure for determining real-time concrete condition, without requiring previous measurements for comparative purposes.

© 2018 Chinese Society of Pavement Engineering. This is an open access article under the CC BY-NC-ND license

(<http://creativecommons.org/licenses/by-nc-nd/4.0/>).

Keywords: Freeze-thaw; Nondestructive testing; Shear waves; Concrete; Durability; Damage detection

1. Introduction

Freeze-thaw damage in concrete structures continues to be a serious issue for infrastructure in regions which experience temperature swings below freezing [1], creating the most persistent problems associated with deterioration to concrete infrastructure in cold weather climates [2]. As such, significant research effort has been devoted to this type of damage [3–7]. Freeze-thaw damage is caused by

expansive pressures resulting from the freezing of excess water present in the concrete microstructure. As a result, microcracking ensues and eventually creates spalling and distress to the concrete system [8].

Resistance of concrete mix to freeze-thaw damage can be measured via standardized tests [9]. This testing involves a beam specimen undergoing multiple rounds of freezing and thawing cycles, combined with periodic measurement of the fundamental transverse frequency and calculation of the Relative Dynamic Modulus of Elasticity, which is used to assess the relative damage condition (i.e. lower Relative Dynamic Modulus of Elasticity values occur after a number of freeze-thaw cycles have occurred and indicates the presence of damage). While this procedure is beneficial

^{*} Corresponding author.

E-mail addresses: kfreese@iastate.edu (K. Freese), lev.k@pitt.edu (L. Khazanovich), kyle.hoegh@state.mn.us (K. Hoegh).

Peer review under responsibility of Chinese Society of Pavement Engineering.

for comparing freeze-thaw resistance of concrete mixes via small laboratory specimens [10], this is an invariable option when considering in-situ conditions and damage detection applications. Additionally, the testing involved in this method does not allow for the location or extent of damage to be determined.

Accurately detecting damage at its initial stages, and before excessive deterioration occurs, is a goal which has yet to be achieved by nondestructive testing techniques. Many nondestructive testing technologies have been employed for general cracking detection purposes, though freeze-thaw damage is of particular interest to this paper. Wave-based nondestructive evaluation techniques have been employed in the past for the detection of microcracking in cement paste. For instance, using diffuse ultrasound, quantitative measures of dissipation and diffusion coefficients can be found based upon the frequency and microstructure of cement-based materials [11]. While the results showed promise for gaining insight as to the propagation of ultrasonic waves in cement-based materials, limitations were present due to sensitivity to diffusivity parameter selections.

Seismic tomography has also been utilized to detect cracking. This method differentiates zones based upon variation in the velocity of compression or P-waves. The seismic tomography analysis was successful in locating a major visible tensile crack in the structure. While this technology showed promise for the detection of damage below the surface, the device employed was only successful in detecting major cracks and thus not ideal for microcrack detection [12].

Nonlinear acoustics, however, were seen to detect and track the formation of microcracks at a promising sensitivity level [13]. The ultrasonic approach enabled the type of damage to be determined based upon granular swelling assessment in order to designate alkali–silica reaction (ASR) damage. While the results showed promise, there are limitations to the approaches used including limited applicability for certain ranges of ASR development and difficulty in detecting the reaction at its early stages. Additionally, the nonlinear parameter is extremely sensitive to microcracking. While this is a valuable asset for damage

detection, the nonlinear parameter is not only sensitive to the number of cracks but also the features of the crack and the level of heterogeneity of the sample. This highlights the need for a method which has high measurement efficiency, accuracy, and decreased subjectivity for concrete damage detection applications.

In this study, shear-horizontal waves were utilized for nondestructive evaluation in order to address the limitations discussed above. Additionally, the utilization of shear waves allows for an analysis which is independent of moisture conditions. The ultrasonic shear velocity array device used for this research employs dry point contact (DPC) transducers capable of deep diagnostics [14]. The specific device utilized, called MIRA [15], is composed of 40 DPC transducers, grouped in 10 channels, which interact as shown in Fig. 1. The wave is emitted from channel 1 transducers and received by the remaining channels, as shown on the left. This same interaction occurs for the remaining transducers, as shown on the right, resulting in 45 unique impulse time histories per measurement. The distance between adjacent transducer channels is 40 mm.

The array setup accommodates multiple transducer pairs which allow for heightened measurement confidence, as well as incorporating redundancy [16–19]. The measurements acquired by this device were used to develop methods for detecting freeze-thaw damage in concrete slabs.

2. Experimental investigation

The Electric Power Research Institute (EPRI) commissioned the fabrication of four slabs with various levels of freeze-thaw damage, with each slab measuring 122 by 91 cm (48 by 36 inches) and 20 cm (8 inches) deep. The mix was prepared with a 0.5 w/c ratio with no air entrainment. After fabrication, the four samples were moist cured for 14 days. The control sample was removed from the curing room and maintained at ambient temperature and relative humidity in the laboratory. The remaining slabs were placed in an environmental chamber and subjected to cycles of freezing and thawing. The cycles consisted of temperatures in the chamber fluctuating between $-20\text{ }^{\circ}\text{C}$ and $12\text{ }^{\circ}\text{C}$ at a relative humidity of approximately 98%. The

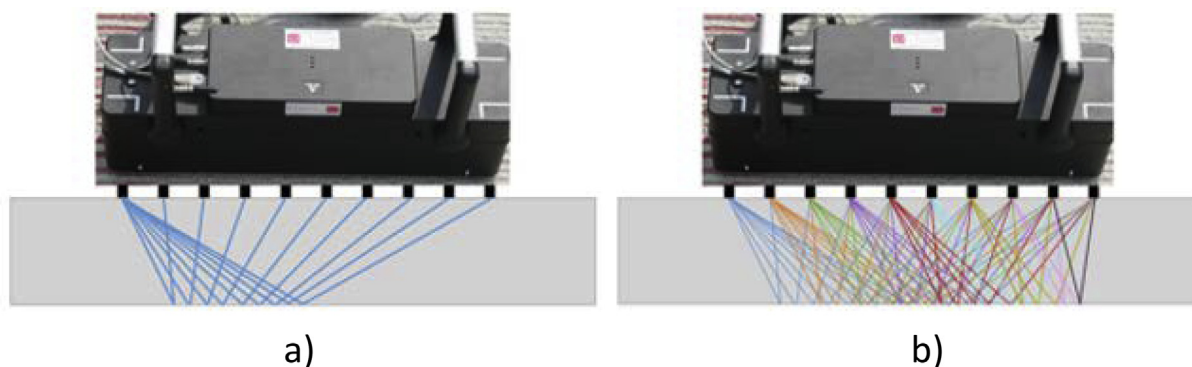


Fig. 1. Transducer interaction from transducer 1 (a) and from all transducers (b) which yields 45 unique impulse time histories.

duration of each cycle was approximately 45 h. A summary of the slabs which were tested is provided here:

- Slab A: no freeze-thaw cycles induced
- Slab B: 72 freeze-thaw cycles induced
- Slab C: 80 freeze-thaw cycles induced
- Slab D: 114 freeze-thaw cycles induced

Corresponding visual survey results for all four slabs are shown in Fig. 2, with crack widths ranging from hairline cracks to 0.3 mm in width. Fig. 3 shows a photo of the condition of slab D, further showing the damage present, as highlighted by chalking.

These four slabs were tested using the ultrasound linear array device, MIRA, shown in Fig. 4 on the left. This device yields 45 individual time histories per individual scan. A total of 66 scans were obtained for each slab, using a one period impulse frequency of 50 kHz. The 36-cm wide scans were taken in sets of 11 positions with a 5 cm step size (allowing for 35 cm of overlap from the previous scan), moving from north to south of each slab. This set of 11 scans was then taken in 6 different locations with a 12.5 cm step size moving east to west, as shown in Fig. 4 on the right. As a result, the surface of the slab was analyzed and redundancy was incorporated via the overlapping nature of the measurement acquisition process. Because of this, an expansive data set containing over



Fig. 3. Photograph of condition of slab D.

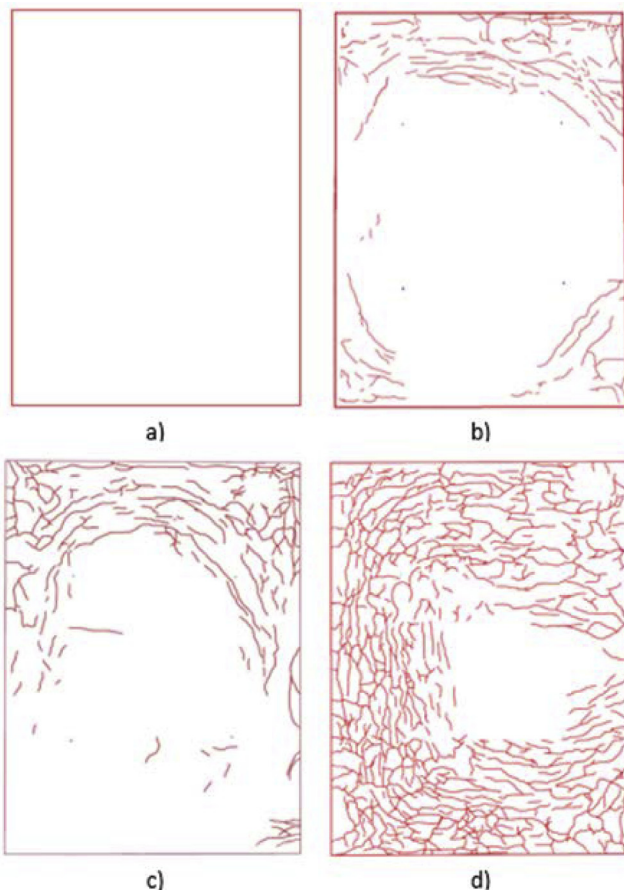


Fig. 2. Visual condition surveys of slabs A, B, C and D.

10,000 impulse time histories was obtained from this analysis.

The ultrasound signals collected via the experimental investigation were analyzed to determine the condition of the concrete slabs. When the surface of the slab is excited by one of the transducers, the wave propagates through the specimen and a portion of the wave will reflect back when it encounters changes in properties, such as inclusions or layer boundaries. An example of a typical signal for sound concrete is shown below in Fig. 5 (left) as well as a cross section which would create this type of response (right). The direct arrival impulse is the result of the wave traveling the shortest distance from one transducer to another, in this case along the surface of the slab. The reflected impulse is the result of the wave reflecting off of the bottom surface of the slab. Each individual scan which is obtained results in the acquisition of 45 unique raw signals. The ultrasound signals collected via the experimental investigation were analyzed using two methods: one which utilized reconstruction images formulated from the array data and another which quantified individual signal characteristics. These methods are described in the following sections, and their respective results are compared both with each other and with the visual survey results.

3. Reconstruction evaluation

The experimental investigation yielded 6 rows of 11 overlapping MIRA scans per slab. The measurements from

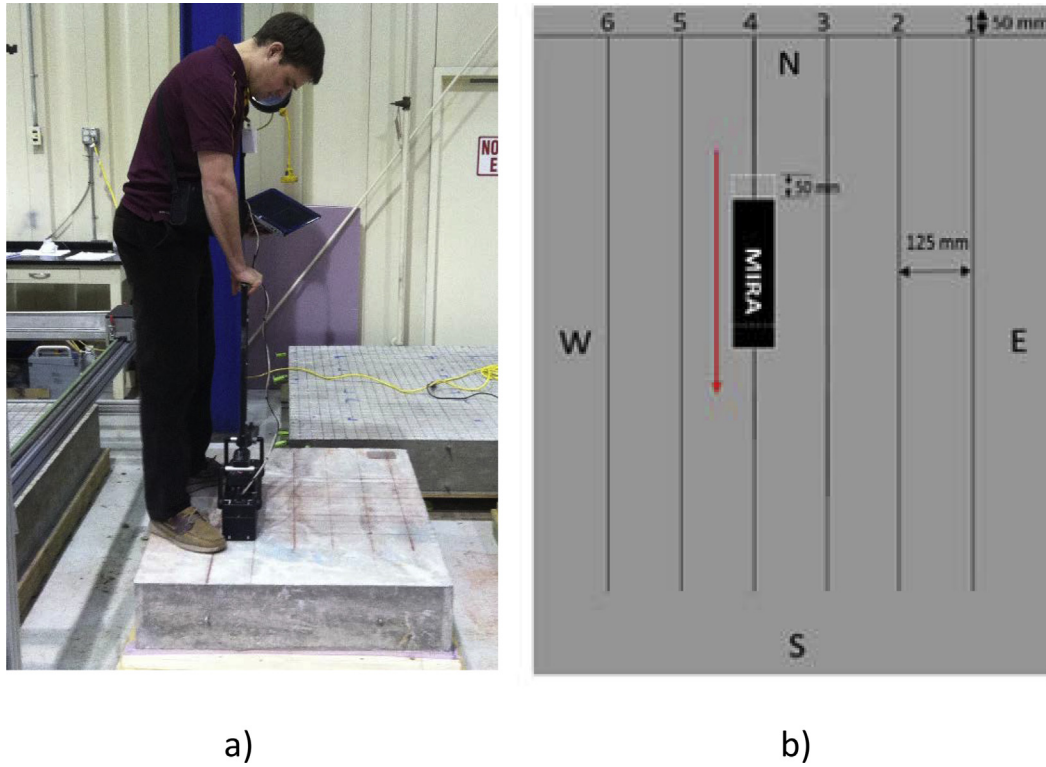


Fig. 4. Experimental investigation setup (a) and schematic of measurement locations (b).

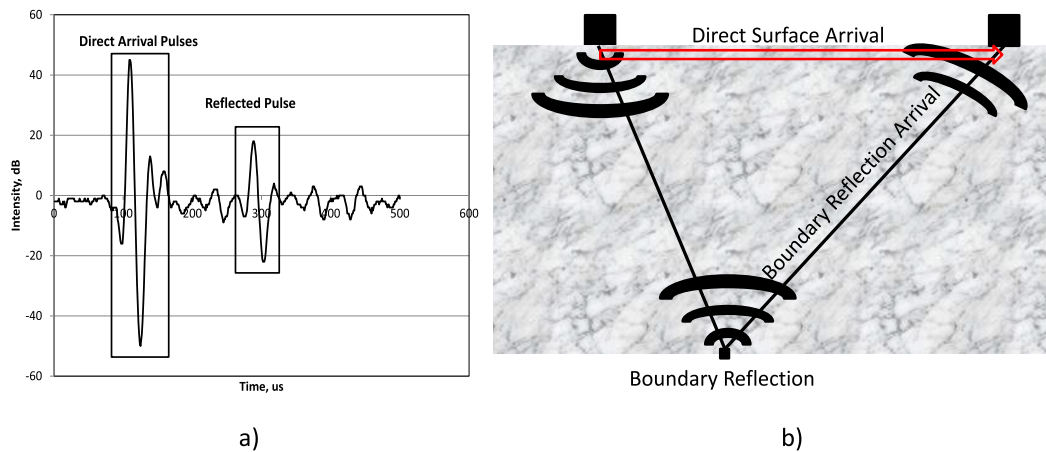


Fig. 5. Sample impulse time history (a) and schematic that would cause this type of response (b) (Hoegh 2013).

each row of scans were used to create panoramic reconstructions. This was achieved via the creation of Synthetic Aperture Focusing Technique (SAFT) reconstructions from reflection portions of the 45 signals from each individual scan. SAFT is a popular emerging technology for the analysis of multiple array data [20–23]. While software included with the device can yield SAFT reconstructions, this study utilized a version of SAFT which was developed at the University of Minnesota [24]. Reconstructions provide focused images which show the presence of damage or inclusions, or in undamaged cases, the presence of only the backwall. Combining these individual SAFT reconstructions into one comprehensive panoramic recon-

struction allows for analysis of the entire cross section and reduced signal to noise effects caused by the heterogeneous nature of concrete [25].

The following equation allows for the creation of the SAFT reconstructions [25–31,24]:

$$\hat{o}(x, z) = \int_{x'_{emin}}^{x'_{emax}} dx'_e \int_{x'_{rmin}}^{x'_{rmax}} A(x'_r, x'_e, x, z) * s \left(x'_r, x'_e, \frac{1}{c} \left(\sqrt{z^2 + (x - x'_e)^2} + \sqrt{z^2 + (x - x'_r)^2} \right) \right) dx'_r \quad (1)$$

where $\hat{\theta}(x, z)$ is the reconstruction image matrix, $A(x_r, x_e, x, z)$ is the apodization factor, e and r differentiate between the emitting and receiving transducer, x'_{\min} and x'_{\max} are the interval in which the signals are measured, c is the sound velocity, x and z are the horizontal and vertical positions in the region of interest (ROI), x' is the transducer location, and s is the received impulse. The apodization factor accounts for the multiple incident angles incorporated by the array. The instantaneous amplitude of the reconstruction can be calculated using Hilbert transform at each vertical coordinate, and results from the following equation:

$$\hat{\theta}^{IA}(x, z) = \sqrt{(\hat{\theta}(x, z))^2 + \left(\frac{1}{\pi} \int_{-\infty}^{\infty} \frac{\hat{\theta}(x, s)}{z - s} ds\right)^2} \quad (2)$$

where $\hat{\theta}^{IA}(x, z)$ is the relative reflectivity and provides the SAFT reconstructions based upon the instantaneous amplitude. More detail on the method used to create SAFT reconstructions can be found in Hoegh and Khazanovich (2015).

However, these SAFT reconstructions have their limitations. The edges of each individual reconstruction span only 400 mm, making comprehensive cross section analysis difficult. To incorporate greater confidence and redundancy via capitalizing on the overlapping nature of the eleven measurements, panoramic reconstructions can improve the results via the compiling of individual SAFT reconstructions. The following equation is used to combine the individual reconstructions to create the panoramic reconstructions which have a larger region of interest:

$$\hat{\theta}_{PAN}^m(x, z) = \begin{cases} \hat{\theta}_{PAN}^{m-1}(x, z), & \text{if } x < D \\ \max(\hat{\theta}_{PAN}^{m-1}(x, z), \hat{\theta}_I^m(x, z)), & \text{if } D < x < x_{PAN}^{m-1} \\ \hat{\theta}_I^m(x, z), & \text{if } x > x_I^m \end{cases} \quad (3)$$

where each SAFT scan, $\hat{\theta}_I^m$, where m is the index of the current SAFT scan and I denotes that it is an individual scan, is combined to form the new region of interest, ROI_{PAN}^m . This region has a vertical dimension of z and a horizontal dimension of x_{PAN}^m , in this case 900 mm, and D is the distance from the global origin [32,24,33]. For each panoramic reconstruction in this study, eleven individual SAFT scans were merged in this manner, as shown in Fig. 6, yielding 6 panoramic reconstructions for each slab.

3.1. Panoramic reconstruction characterization

Visual analysis of the panoramics showed differences in the slab condition, most prominently through the presence of the backwall reflection (or the reflection caused by the bottom surface of the slab). This backwall presence is expected due to the sound condition of the concrete and lack of relative reflection prior to this depth. From Eqs. (1)–(3), the magnitude of the backwall reflection depends

on the number of sensors in the array system and the magnitude of the recorded signal (reported in dBa by the device utilized for this research) from individual sending and receiving pairs due to reflection from the bottom of the slab. The latter depends on the contact condition between the sensors and the surface of the concrete, as well as the pressure applied to the device. Thus, only relative values and not absolute magnitudes are of importance. A typical scan on sound concrete (Slab A) is shown in Fig. 7. The yellow regions of the reconstruction indicate areas of increased reflectivity, caused by changes in acoustic impedance, such as the backwall presence at a depth of ~ 200 mm. The backwall presence is consistently strong, indicating strong relative reflection at the thickness interface as compared to its shallower features when evaluating the SAFT panoramic reconstructions. In other words, there is no damage present.

With conditions such as those shown in Fig. 7 serving as the sound or reference case, categories could be created based upon deviations from this case. The following three categories were observed: (1) sound: reconstructions showing a strong and continuous relative reflectivity at the backwall; (2) partial damage: reconstructions exhibiting a strong backwall reflection at selected locations along with features indicating the presence of damage such as a discontinuity in the backwall reflection; (3) damaged: reconstructions showing no presence of a backwall reflection. Since this initial categorization is very general, it allows for reconstructions that are visually different to fit in the same category. To show the variation of reconstructions within a category and give a background in the indications used to categorize the sections, two examples of the partially damaged and fully damaged conditions are given below along with a description.

Figs. 8 and 9 show example reconstructions indicating a slightly damaged concrete condition. Fig. 8 was taken on the West side of slab B (5th SAFT-Pan). It shows a mostly sound concrete condition with a continuous and uniform backwall reflection in the middle and right side of the reconstruction. However, the lack of a backwall reflection on the leftmost (North) portion and a shift deeper in the backwall reflection on the left indicates the presence of damage. In this case, attenuation from damage could have shadowed the backwall in the former observation and increased the travel path in the latter. Fig. 9 was taken in the middle of slab B (3rd and 4th SAFT-Pans). While both scans showed a shift in the backwall reflection deeper in the center, the scan taken at the 3rd SAFT-Pan (top) also shows direct reflections at a shallower depth, both indicating damaged concrete. However, these scans were still categorized as only slightly damaged, since portions on the left and right showed a strong backwall reflection.

Figs. 10 and 11 show example reconstructions indicating a damaged concrete condition. Fig. 10 shows a scan taken in the middle of slab D (3rd SAFT-Pan). It shows a high reflectivity throughout the reconstruction and absence of a backwall reflection indicating the presence of damage.

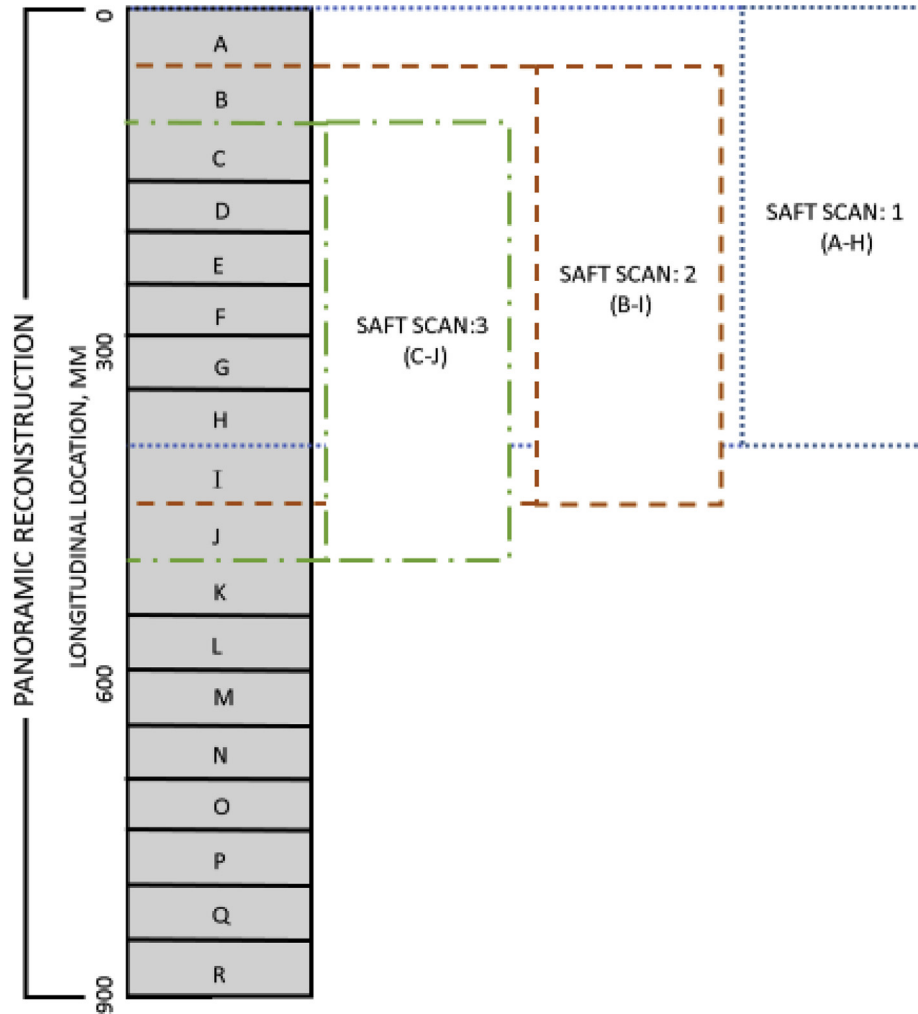


Fig. 6. Panoramic reconstruction compilation schematic.

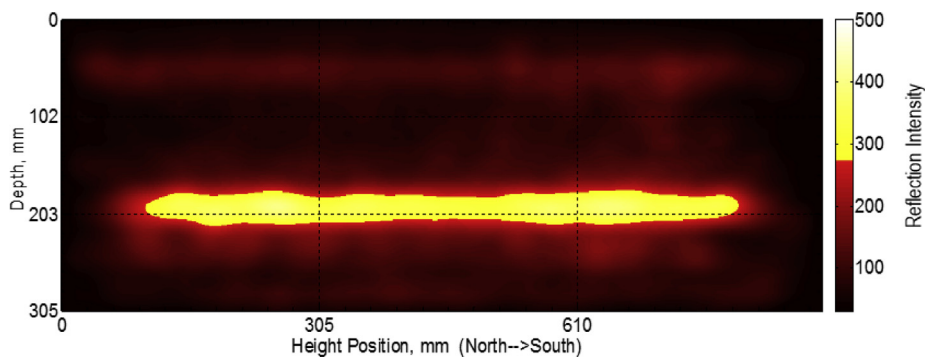


Fig. 7. Reconstruction in the middle of slab A indicating sound concrete condition.

Fig. 11 shows a scan taken on the west side of slab D (5th SAFT-Pan). Both scans showed a lack of a backwall reflection, either due to prohibitive noise at shallow depths or attenuation of the signal prior to arrival at the concrete depth interface, indicating damaged concrete. It is also worth noting that if regions of the upper layer of the concrete are severely damaged, then zones exhibiting significantly lower stiffness are present. This may cause multiple

secondary reflections which can appear on the SAFT reconstruction as irregular damage zones, not necessarily corresponding to the boundaries of the damaged area. This illustrates that SAFT techniques which are intuitive for planar defects and inclusions parallel to the surface (Hoegh and Khazanovich 2015) may lead to misinterpretation if applied to specimens with irregular damage present near the surface.

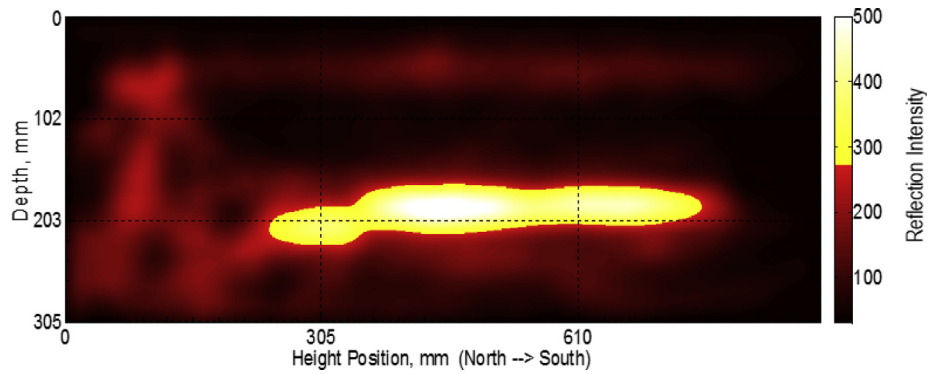


Fig. 8. Reconstruction on the west side of slab B, indicating partially damaged concrete.

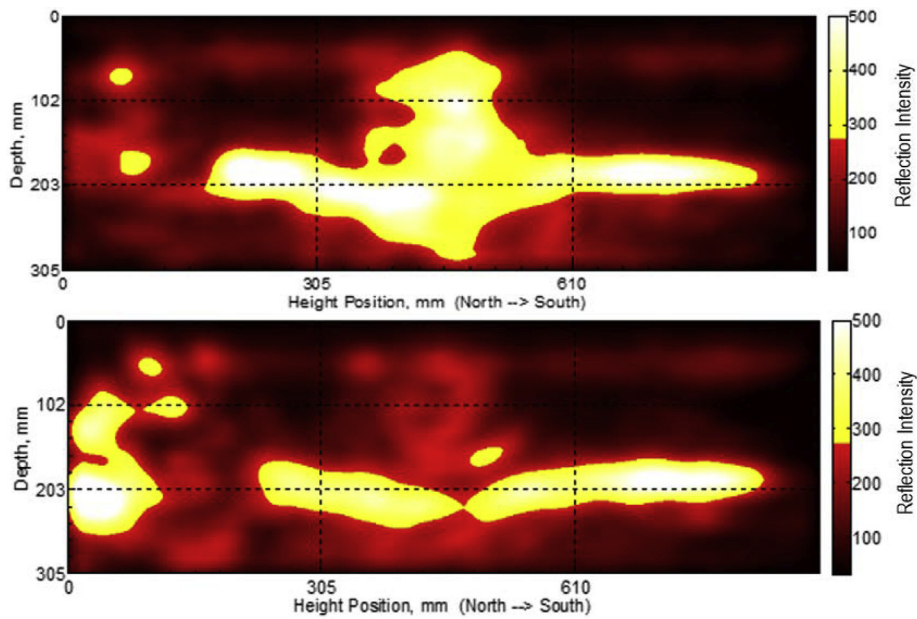


Fig. 9. Reconstructions in the middle of slab C indicating partially damaged concrete condition.

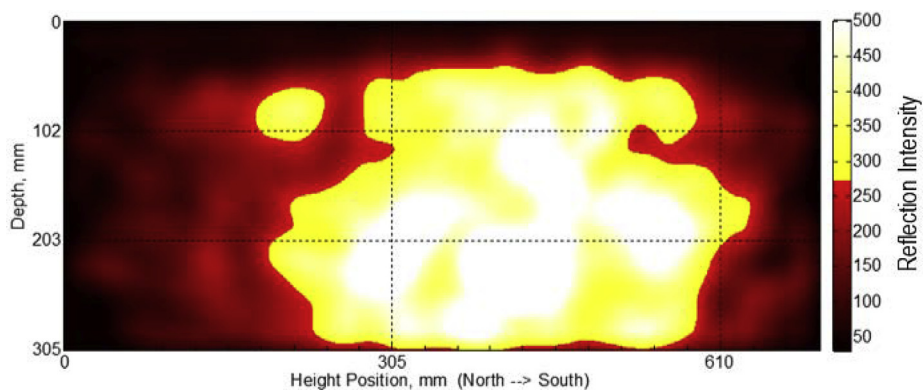


Fig. 10. Reconstruction in the middle of slab D indicating damaged concrete condition.

4. Quantitative evaluation

While the panoramic reconstructions provide valuable qualitative information regarding the condition of the con-

crete, a quantitative analysis is desirable due to the objectiveness and efficiency of the results. The qualitative analysis requires subjective decisions, such as threshold selection and visual inspection, but the quantitative

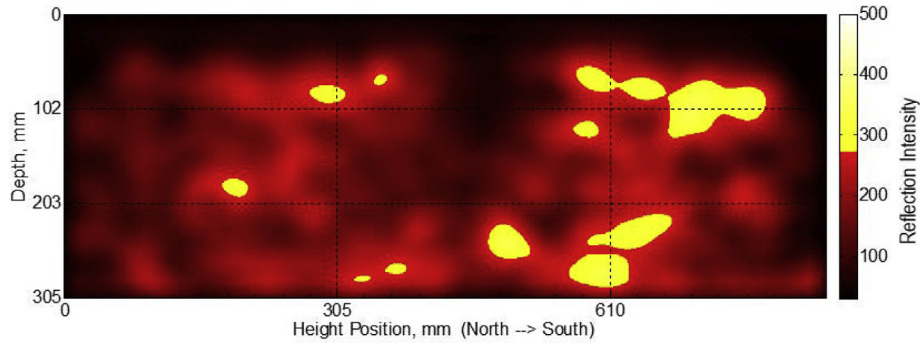


Fig. 11. Reconstruction from the west side of slab D indicating damaged concrete condition.

method suggested here is completely objective and utilized identical analytic variables for all scans.

The same impulse time histories which were implemented in the reconstruction analysis were utilized for the subsequent numerical analysis. As previously described, the linear array system which was used for testing creates an output of 45 unique impulse time histories. These raw data were used in order to perform a signal analysis. Visual investigation of the signals showed drastic differences in signal shapes for different slab conditions, as shown in Fig. 12. The control, shown on the left, is an example of a normalized raw signal for sound concrete, while the freeze-thaw condition shown on the right is representative of damaged concrete. The two key differences between these signals are the shape of the direct arrival impulse (highlighted in blue), and the increased oscillation which occurs after the direct arrival (highlighted in orange).

4.1. Hilbert transform indicator development

The numerical indicator presented in this paper is based upon the instantaneous amplitude envelope that is created using Hilbert transform. Hilbert transform is a common signal analysis method, valuable for determining instantaneous attributes. The Hilbert transform, $HT(t)$ of a function, $f(t)$ is commonly defined as:

$$HT(t) = \sqrt{(f(t))^2 + \left(\frac{1}{\pi} \int_{-\infty}^{\infty} \frac{f(\tau)}{t - \tau} d\tau\right)^2} \quad (4)$$

This instantaneous amplitude envelope served as the basis for the creation of a numerical indicator capable of detecting the signal differences outlined previously. The indicator, named the Hilbert Transform Indicator (HTI), is shown below in Eq. (5).

$$HTI = \int_0^{500} \frac{HT(t)}{HT_{max}} dt \quad (5)$$

where HT_{max} is the maximum value of the function $HT(t)$ in the interval from 0 to 500 microseconds. A time window of 500 microseconds was selected to ensure that the direct arrival impulse as well as all subsequent oscillations were captured. Normalizing of the data to remove magnitude dependence was the result of a thorough visual investigation of the signals, which revealed that the magnitude of the signal was not correlated to the condition of the concrete. This equation is applied to all transducer pairs of each impulse time history.

To illustrate the effect of damage on the Hilbert transform envelope, as well as on the subsequent HTI results, consider two sample normalized envelopes graphed in Fig. 13. In blue, the normalized Hilbert transform envelope for a signal taken on sound concrete is shown, while a signal from a damaged concrete slab is shown in orange. The HTI results were 55 and 137, for the sound and damaged

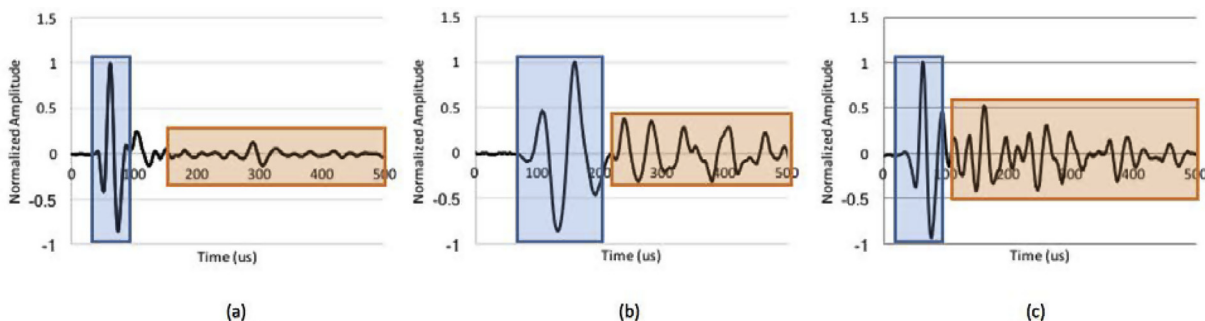


Fig. 12. Example of clean (a) and damaged (b and c) raw signals.

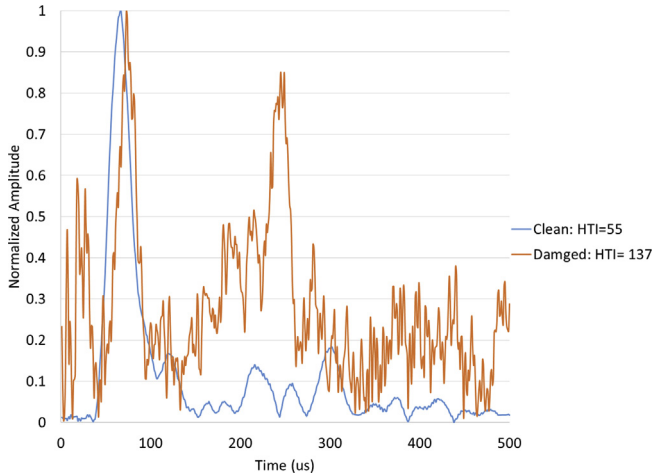


Fig. 13. Normalized Hilbert transform envelopes for sound and damaged concrete.

slabs, respectively. This increase in HTI for the damaged slab is the result of the increase in instantaneous amplitude envelope, made obvious by comparing it to the sound concrete condition. As such, higher HTI values are indicative of declining conditions of the specimen.

4.2. HTI characterization

In order to incorporate redundancy and provide increased measurement confidence, the HTI values which are provided here are the result of averaging all 45 values to provide one more accurate designation per scan. These HTI values are shown in Fig. 14. The color maps shown utilize a gradient in which white is indicative of the lowest HTI value seen (in this case, 62) and darker shades are indicative of the highest HTI value seen (in this case, 182). In other words, white or very light sections are representative of concrete in sound condition, while darker shades would indicate damaged concrete. In general, an HTI value less than 90 is indicative of concrete which is in good condition. This threshold was determined based upon an extensive analysis of undamaged data from prior projects and is independent of mix design or other variables. As can be seen, the HTI values seem to capture the presence of damage accurately. Slab A, the undamaged slab, is the lightest in color and contains HTI values of 94 or less. Slab D, the most damaged slab, is the darkest in color with a minimum HTI value of 106 and a maximum value of 182. Slabs B and C have conditions ranging from sound to damaged, as would be expected, with slab C in a more damaged state than slab B.

While the progression of damage level in the slab data set is apparent, there are other trends that can be seen. In general, the greatest HTI values are those which are in the corners or edges of the slab. This can be explained via two rationales. The first of which involves the effects of edges on the ultrasound measurements. Because of the presence of vertical surfaces on the edges of the specimen, there is a potential for waves to reflect from these surfaces

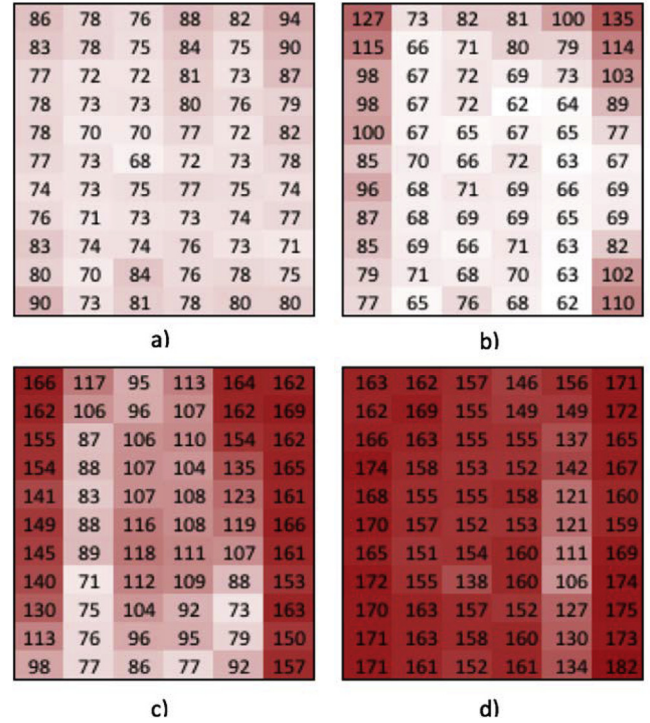


Fig. 14. HTI color maps for: slab A, clean slab; slab B, partially damaged; slab C, partially damaged; and slab D, damaged.

and create added distortion in the response of the recorded signal. This can create slightly increased HTI values, though not significant. The greater justification for these increased values is the behavior of freeze-thaw damage. Water is most quickly absorbed via joints and edges due to their increased surface area and water penetration capabilities. As a result, freeze-thaw damage generally initiates at the edges or at pavement joints and moves inward, thus confirming the trend of greater HTI values present along the perimeter. These results can also be confirmed via comparing the HTI results to the visual survey results previously shown in Fig. 2. The areas which exhibit higher HTI values correspond well with the areas of the slabs which exhibited visual signs of damage.

It should be noted that the magnitudes of the HTI values discussed in this research are only applicable when the same device settings (i.e. shear-horizontal wave impulse frequency and duration) are utilized. However, the results seen were independent of contact and surface conditions, as well as concrete mix properties, and the device settings are widely applicable to concrete structures [34].

5. Results

Both methods described previously produced categorized damage results for the slabs in a nondestructive manner. To compare the results of both analyses, the panoramic reconstructions are presented in conjunction with the HTI values which resulted from the numerical analysis. The results for this comparison are shown for slab B in Fig. 15 and slab C in Fig. 16. These figures show the

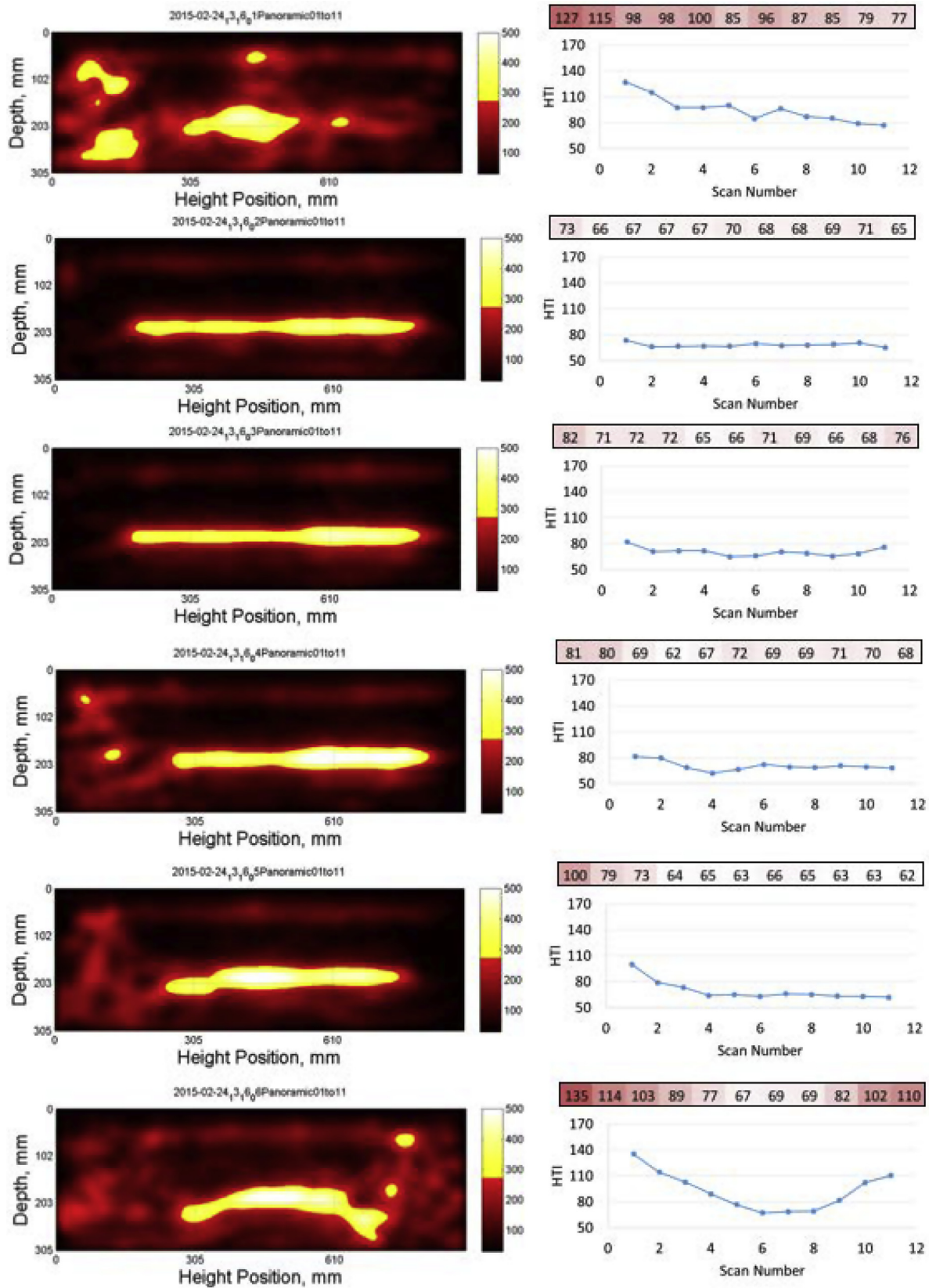


Fig. 15. Comparison of panoramic reconstructions (left) and HTI index (right) analyses for slab B.

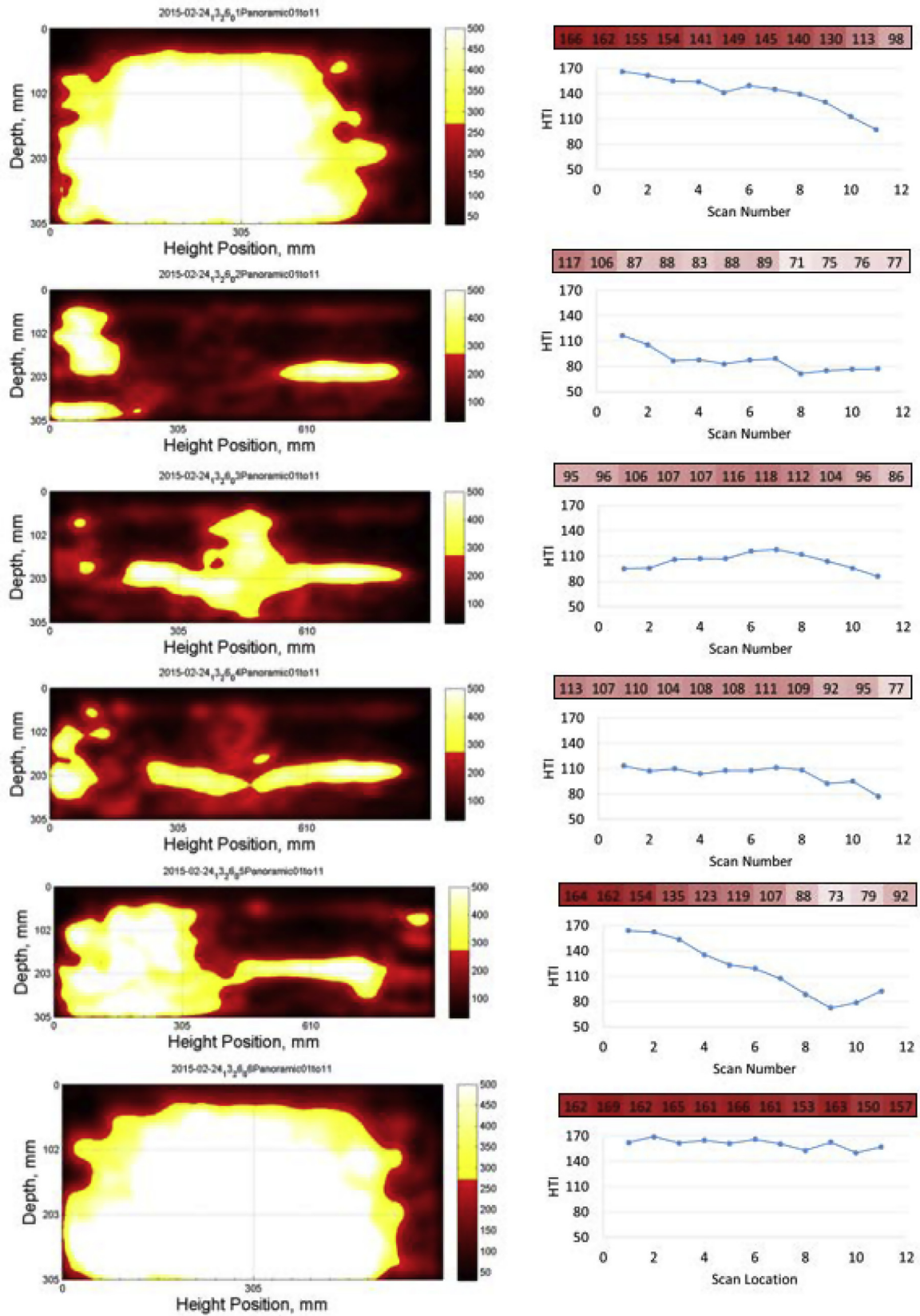


Fig. 16. Comparison of panoramic reconstructions (left) and HTI index (right) analyses of slab C.

six panoramic reconstructions on the left, with the HTI values for the same slab location shown both numerically and graphically on the right. The horizontal axis of the panoramic reconstructions, “Height Position”, corresponds to the actual location along the surface of the slab from north to south. The horizontal axis of the HTI graphs corresponds to the scan number from 1 to 11. These axes are essentially the same, as the scans were taken in numerical order from north to south, aligning with the height position. Again, HTI values with dark shades indicate damaged concrete, while lighter shades indicate sound concrete.

As can be seen from these figures, the HTI values show the same damage trends that can be deduced via the backwall presence in the reconstructions. For example, the bottom (sixth) panoramic reconstruction in Fig. 15 shows that the backwall was not as apparent on the north and south regions, but was present in the center of the slab. The HTI results for the same scans show higher HTI values (over 100) for these same outer regions, while HTI values indicated sound concrete in the center (values in the 60 s and 70 s). As such, both methods showed that concrete was in sound condition in the center of the slab, but damage was present in the north and south regions. Conversely, the second and third panoramic and HTI results shown in Fig. 15 indicate sound concrete throughout the entirety of that portion of the slab, as indicated by a strong backwall presence and consistently low HTI values. To summarize the condition of slab B, the 2nd and 3rd panoramics and HTI values showed sound concrete, while the remaining four sections showed signs of partially damaged concrete.

The same similarities can be seen in the results for slab C. The most damaged panoramics shown in Fig. 16 are the first and sixth reconstructions. These scans also resulted in high HTI values, as indicated by the dark shading of the HTI color maps shown. Additionally, the fifth panoramic showed considerable damage on the left (north) side of the slab, with concrete in good condition on the right (south). These same trends are seen in the HTI color map and graph. The results for both slab D and slab A also showed very good agreement. These cases are not shown here for simplicity, as the scans were either all damaged or all sound. Instead, the intricacies of the intermediate partially damaged slabs were shown to highlight the robustness of the analyses presented.

5.1. Summarized slab characterizations

As a result of the visual interpretation of all 24 panoramic reconstructions (6 panoramics per slab, each consisting of 11 individual scans), the condition of the slabs could be qualitatively determined via the diagnosis procedure discussed previously in Section 3.1. All six panoramics for slab A had strong backwall presence and were deemed sound. Slab B had two reconstructions showing sound concrete and 4 reconstructions showing partially damaged conditions. Slab C had 2 reconstructions indicating partially damaged concrete and four reconstructions indicat-

ing damaged concrete. Finally, all six panoramic reconstructions of slab D were considered damaged, with no backwall presence. Additionally, more detailed conditions within each slab can be observed via trends in damaged locations. For example, the north side of the slabs generally showed greater damage levels than the south side. These same trends and damage categorizations were seen in the quantitative analysis results as well. The HTI values captured the same damage presence, without requiring visual interpretation.

The results of the qualitative and quantitative analyses can then be compared to the actual crack patterns demonstrated by the sample test slabs to confirm the results. The survey results shown in Fig. 2 confirm the results of both analyses. When comparing Figs. 15 and 2, the same damage trends can be seen in the slabs, which were further confirmed via the qualitative analysis. Additionally, the trends of increased damage on the northern portion of the slabs were confirmed via the visual surveys. Moreover, the survey of slab D (d) shows that no visible damage was present in the center portion of the slab, while the quantitative analysis indicates that the concrete in this area is not sound with HTI values of over 100 for the entire slab. This shows promise for detecting damage prior to its appearance at the surface.

6. Conclusions

The methods presented in this paper were implemented in order to categorize the damage level within concrete slabs with varying levels of freeze-thaw damage. While the two methods employed vary in their analysis type, they both utilize the same signal data obtained by an ultrasonic shear wave linear array device. Both methods were successful in determining the presence of damage in a noninvasive and efficient manner. The qualitative analysis of the panoramic reconstructions highlighted specific slab areas in which damage was causing shadowing of the backwall, while the quantitative analysis utilized the effect of damage on signal shape in order to numerically indicate the condition of the concrete.

In addition to providing localized damage characterizations, both methods are advantageous from a confidence standpoint as well. The panoramic reconstructions utilize overlapping scans, adding redundant measurements to increase measurement assurance. The quantitative indicator, HTI, is based upon the numerical analysis of all 45 impulse time histories from each scan. As a result, the sample set is large and produces confidence in the indicator.

Moreover, the HTI method can be implemented on in-situ concrete pavements for determining real-time concrete condition, without requiring previous measurements for comparative purposes. As a result, the applications of this technique are vast. The results of this study show promise for the implementation of methods which can characterize the condition of concrete in an efficient and nondestructive manner.

Acknowledgements

This research was supported by the Federal Highway Administration USDOT Grant DTRT13-G-UTC44. The authors would like to acknowledge the contribution of Dr. Eric Gianini from the University of Alabama for preparing and conditioning the samples.

References

- [1] C. Korhonen, New developments in cold-weather concreting, in: Proceedings, The 11th International Conference of Cold Regions Engineering, 2002, pp. 531–537.
- [2] J. Tanesi, R. Meininger, Freeze-thaw resistance of concrete with marginal air content, FHWA-HRT-06-117, Federal Highway Administration, Washington, DC, 2006, pp. 83.
- [3] Z. Yang, *Assessing Cumulative Damage in Concrete and Quantifying its Influence on Life Cycle Performance Modeling* (Doctoral dissertation), Purdue University, 2004.
- [4] Y. Farnam, D. Bentz, A. Sakulich, D. Flynn, J. Weiss, Measuring freeze and thaw damage in mortars containing deicing salt using a low-temperature longitudinal guarded comparative calorimeter and acoustic emission, *Adv. Civ. Eng. Mater.* 3 (1) (2014) 23.
- [5] W. Li, M. Pour-Ghaz, J. Castro, J. Weiss, Water absorption and critical degree of saturation relating to freeze-thaw damage in concrete pavement joints, *J. Mater. Civ. Eng.* (2012), [https://doi.org/10.1061/\(ASCE\)MT.1943-5533.0000383](https://doi.org/10.1061/(ASCE)MT.1943-5533.0000383), 299–307.
- [6] C. Hazaree, K. Wang, H. Ceylan, K. Gopalakrishnan, Capillary transport in RCC: water-to-cement ratio, strength, and freeze-thaw resistance, *J. Mater. Civ. Eng.* (2011), [https://doi.org/10.1061/\(ASCE\)MT.1943-5533.0000284](https://doi.org/10.1061/(ASCE)MT.1943-5533.0000284), 1181–1191.
- [7] J.N. Eiras, T. Kundu, J.S. Popovics, J. Monzó, M.V. Borrachero, J.J. P. Bernabeu, Monitoring material nonlinearity and attenuation variations in mortar subjected to freezing-thawing cycles, in: Proceedings of Meetings on Acoustics, vol. 20, no. 1, Acoustical Society of America, 2015, p. 065001.
- [8] Z. Yang, W.J. Weiss, J. Olek, Water transport in concrete damaged by tensile loading and freeze–thaw cycling, *J. Mater. Civ. Eng.* (2006)
- [9] ASTM Standard C666, Standard Test Method for Resistance of Concrete to Rapid Freezing and Thawing, ASTM International, West Conshohocken, PA, 2015, 10.1520/C0666_C0666M-15, www.astm.org.
- [10] S. Wang, E. Llamazos, L. Baxter, F. Fonseca, Durability of biomass fly ash concrete: freezing and thawing and rapid chloride permeability tests, *Fuel* 87 (3) (2008) 359–364.
- [11] J. Becker, L.J. Jacobs, J. Qu, Characterization of cement-based materials using diffuse ultrasound, *J. Eng. Mech.* 129 (2003) 1478–1484.
- [12] P. Rivard, G. Ballivy, C. Gravel, F. Saint-Pierre, Monitoring of an hydraulic structure affected by ASR: a case study, *Cem. Concr. Res.* 40 (4) (2010) 676–680.
- [13] Y. Boukari, D. Bulteel, P. Rivard, N.E. Abriak, Combining nonlinear acoustics and physico-chemical analysis of aggregates to improve alkali–silica reaction monitoring, *Cem. Concr. Res.* 67 (2015) 44–51.
- [14] V.G. Shevaldykin, A.A. Samokrutov, V.N. Kozlov, Ultrasonic low-frequency transducers with dry dot contact and their applications for evaluation of concrete structures, *IEEE Ultrason. Symp. Proc.* 1–2 (2002) 793–798.
- [15] A. Bishko, A. Samokrutov, V. Shevaldykin, Ultrasonic echo-pulse tomography of concrete using shear waves low-frequency phased antenna arrays, in: Proceedings of the 17th World Conference on Nondestructive Testing, vol. 25, no. 28.10, 2008.
- [16] K. Hoegh, L. Khazanovich, Correlation analysis of 2D tomographic images for flaw detection in pavements, *J. Testing Eval. Am. Soc. Testing Mater.* 40 (2012) 3.
- [17] K. Hoegh, L. Khazanovich, Concrete pavement joint diagnostics using ultrasonic tomography, *Transp. Res. Rec.: J. Transp. Res. Board* 2305 (2012) 54–61.
- [18] K. Hoegh, L. Khazanovich, K.R. Maser, N. Tran, Evaluation of ultrasonic technique for detecting delamination in asphalt pavements, in: Transportation Research Board 91st Annual Meeting, 2012.
- [19] K. Hoegh, T. Yu, L. Khazanovich, Ultrasonic tomography technique for evaluation of concrete pavements, *Transp. Res. Rec.: J. Transp. Res. Board* 2232 (2011) 85–94.
- [20] A. Ganguli, C.M. Rappaport, D. Abramo, S. Wadia-Fascetti, Synthetic aperture imaging for flaw detection in a concrete medium, *NDT&E Int.* 45 (2012) 79–514, <https://doi.org/10.1016/j.ndteint.2011.09.004> 515.
- [21] K.J. Langenberg, M. Berger, Th. Kreutter, K. Mayer, V. Schmitz, Synthetic aperture focusing technique signal processing, *NDT Int.* 19 (3) (1986) 177–189, [https://doi.org/10.1016/0308-9126\(86\)90107-0](https://doi.org/10.1016/0308-9126(86)90107-0) 518.
- [22] M. Spies H. Rieder A. Dillhöfer V. Schmitz W. Müller Synthetic aperture focusing and time-of-flight diffraction ultrasonic imaging—past and present *J. Nondestruct. Eval.* 2012 31 310 323 10.1007/s10921-012-0150-z
- [23] M. Schickert, M. Krause, W. Müller, Ultrasonic imaging of concrete elements using reconstruction by synthetic aperture focusing technique, *J. Mater. Civ. Eng.* 15 (2003) 235–246, Permalink: [http://dx.doi.org/10.1061/\(ASCE\)0899-1561\(2003\)15:3\(235\)](http://dx.doi.org/10.1061/(ASCE)0899-1561(2003)15:3(235)).
- [24] K. Hoegh, L. Khazanovich, Extended synthetic aperture focusing technique for ultrasonic imaging of concrete, *NDT & E Int.* 74 (2015) 33–42, <https://doi.org/10.1016/j.ndteint.2015.05.001>.
- [25] K. Langenberg, R. Marklein, K. Mayer, *Ultrasonic Nondestructive Testing of Materials: Theoretical Foundations*, CRC Press, 2012.
- [26] F. Lingvall, T. Olofsson, T. Stepinski, Synthetic aperture imaging using sources with finite aperture: deconvolution of the spatial impulse response, *J. Acoust. Soc. Am.* 114 (1) (2003) 225–234, <https://doi.org/10.1121/1.1575746>.
- [27] J. Qi, J.H. Miao, Y.X. Xie, Synthetic aperture focusing technique and contrast source inversion algorithm applied in elastic wave imaging, *Adv. Mater. Res.* 340 (2012) 402–408.
- [28] S.H. Gray, C.H. Nofors, N.H. Bleistein, Imaging using multi-arrivals: Gaussian beams or multi-arrival Kirchhoff? in: 2002 SEG Annual Meeting, 2002.
- [29] V. Schmitz, S. Chakhlov, W. Müller, Experiences with synthetic aperture focusing technique in the field, *Ultrasonics* 38 (2000) 731–738.
- [30] J.F. Claerbout, *Earth Soundings Analysis: Processing Versus Inversion*, Blackwell Scientific Publications (2004).
- [31] T. Stepinski, An implementation of synthetic aperture focusing technique in frequency domain, *IEEE Trans. Ultrasonics Ferroelectric. Frequency Control* 54 (2007) 1399–1408.
- [32] K. Hoegh, *Ultrasonic Linear Array Evaluation of Concrete Pavements* (Thesis dissertation), University of Minnesota, 2013.
- [33] K. Freeseaman, L. Khazanovich, K. Hoegh, A. Nojavan, A.E. Schultz, S. Chao, Nondestructive monitoring of subsurface damage progression in concrete columns damaged by earthquake loading, *Eng. Struct.* 114 (2016) 148–157, <https://doi.org/10.1016/j.engstruct.2016.02.017>.
- [34] K. Freeseaman, K. Hoegh, L. Khazanovich, Characterization of concrete at various freeze-thaw damage conditions using SH-waves, in: Proceedings of the 42nd Review of Progress in Quantitative Nondestructive Evaluation (QNDE), Minneapolis, MN, July 26–31, 2015.